

Full paper

POM-based metal-organic framework/reduced graphene oxide nanocomposites with hybrid behavior of battery-supercapacitor for superior lithium storage

Tao Wei^{a,1}, Mi Zhang^{a,1}, Ping Wu^a, Yu-Jia Tang^a, Shun-Li Li^{a,*}, Feng-Cui Shen^a, Xiao-Li Wang^a, Xin-Ping Zhou^b, Ya-Qian Lan^{a,*}

^a Jiangsu Key Laboratory of Biofunctional Materials, Jiangsu Key Laboratory of New Power Batteries, School of Chemistry and Materials Science, Nanjing Normal University, Nanjing 210023, PR China

^b College of Chemistry and Chemical Engineering, China University of Mining and Technology, Xuzhou 221116, PR China

ARTICLE INFO

Keywords:

POM-Based MOF
RGO Nanocomposites
Hybrid Behavior of Battery-Supercapacitor
Lithium Storage
Ultra-Stable

ABSTRACT

The energy storage field has witnessed a dramatic expansion in research at materials that might combine the high energy density of batteries and short charging times of supercapacitors. However, the materials mainly focus on transition metal oxides or sulfides, new material has rarely been reported yet. Herein, we report a novel nanocomposite based on polyoxometalates-based metal-organic frameworks (POMOFs)/reduced graphene oxide (RGO) for lithium-ion batteries. It demonstrates the advantages of polyoxometalates (POMs), metal-organic frameworks (MOFs) and RGO, thus shows the hybrid behavior of battery and supercapacitor. A reversible capacity of 1075 mAh g⁻¹ was maintained after 100 cycles, and the capacity retentions are nearly 100% both at 2000 and 3000 mA g⁻¹ for over 400 cycles. These performances are almost the best compared to the reported pristine MOFs and POMs based materials to date. The design and synthesis of POMOFs/RGO nanocomposites might guide the development of new generation electrode materials for lithium-ion batteries.

1. Introduction

Electrochemical energy storage (EES) devices play an increasingly critical role for the upcoming era of portable electronics, electric vehicles, and hybrid electric vehicles in our daily life and energy-intensive society [1–4]. Currently, the two major EES devices are lithium-ion batteries (LIBs) and supercapacitors. In LIBs, the insertion of Li⁺ that enables redox reactions in bulk electrode materials can provide high energy density, but the insertion of Li⁺ is diffusion-controlled and the processes are slow. The supercapacitors store electrostatic energy through the formation of electrical double layer capacitors at electrode interfaces, the processes are controlled by the surface adsorption, so the supercapacitors enable high rate performances but with low energy density. Hence, it is of great significance to design one single EES device which combines battery-like energy and supercapacitor-like rate performances. Inspiringly, pseudocapacitance [5,6] has been witnessed in some transition metal oxides and sulfides as electrodes for LIBs, such as MnO/RGO [4], V₂O₅ [7,8], Fe₂O₃ [9] and ZnS [10] etc. And this sheds light on designing materials for LIBs with hybrid behavior of battery and supercapacitor. Unfortunately,

During cycling of Li⁺ insertion/deinsertion, transition metal oxides typically break into small metal clusters because they can react with Li to form Li₂O, leading to a large volume expansion and a destruction of the structure upon electrochemical cycling, especially at high rates, thus resulting in severe loss of capacity with cycling and a poor electrical conductivity [11,12]. Therefore, it remains a significant challenge to develop new electrode materials with hybrid behavior of battery and supercapacitor for LIBs.

Metal-organic frameworks (MOFs) are a class of porous materials first defined by Yaghi and co-workers [13], which recently have attracted extensive research interests both in LIBs and supercapacitors [14–21]. For example, Tarascon et al. have done pioneering work on the use of MIL-53 (Fe) as a cathode material [22]. Besides, Kang and Yaghi et al. have reported 23 kinds of different MOFs doped with graphene as supercapacitors, and several members of them give high capacitances [23]. Simultaneously, polyoxometalates (POMs) with multi-electron redox properties, stability, and structural diversity are well-suited to achieve a high capacity for energy storage applications (LIBs and pseudocapacitance) [24–28]. A case in point is that theoretical and experimental approach revealed that [PMo₁₂O₄₀]³⁻

* Corresponding authors.

E-mail address: yqlan@njnu.edu.cn (Y.-Q. Lan).

¹ These authors contribute equally to this work.

(PMO₁₂) is endowed as an “electron sponge” due to its large electron uptake number when used as the cathode of LIBs [25]. Thus, high-performance electrode materials with hybrid behavior of battery and supercapacitor for LIBs might be obtained if we combine the advantages of MOFs and POMs together, i.e., POM-based MOFs (POMOFs) [29]. Just as important, because of the poor electronic conductivity of POMOFs, a conducting substrate such as reduced graphene oxide (RGO) is necessary for POMOFs-based electrode materials. To the best of our knowledge, there has rarely been research to integrate MOFs, POMs and graphene for LIBs.

In this work, we firstly synthesized POMOFs/RGO nanocomposites for LIBs by a facile one-pot method. We chose H₅PMO₁₀V₂O₄₀ (PMO₁₀V₂), copper acetate (Cu(OAc)₂·H₂O), 1,3,5-benzenetricarboxylic acid (H₃BTC), and GO to synthesize POMOFs/RGO for the following reasons: (1) Keggin-type heteropolyanions (POMs) are most widely studied in POM chemistry because of the unique structures, good stabilities and reversible redox properties. Compared to PMO₁₂, PMO₁₀V₂ has stronger redox properties because substituting two Mo (VI) atoms in the Keggin cluster for V (V) atoms has been verified to increase the redox potential of the first electron transfer reaction [30]. (2) To support PMO₁₀V₂ molecules, it is necessary for MOFs to possess suitable cavities with the proper size and shape, mild synthesis conditions and high stabilities. Actually, HKUST-1 synthesized using the precursors of Cu²⁺ and H₃BTC, as the well-known and classic MOFs, can meet the above mentioned criteria perfectly. (3) RGO films are also employed here for its excellent intrinsically conductivity, which can be used as the excellent supports and to avoid the agglomeration of the nano-POMOFs particles. Nano-sized POMOFs particles obtained from PMO₁₀V₂, Cu²⁺, H₃BTC can be distributed homogeneously on the flaky RGO films to achieve POMOFs/RGO nanocomposites easily. What's more, in the POMOFs/RGO nanocomposite structures, the porous characteristics of HKUST-1 can buffer the volume expansion induced by the insertion/extraction of Li⁺ and alleviate the stress, which possibly benefits the cycling stability of the LIBs. Meanwhile, PMO₁₀V₂ provide redox reaction sites and RGO conducts the electrons, both of which promote the performances of LIBs obviously. Thus, when the nanocomposites were used as anodes for LIBs, it shows a reversible capacity in excess of 1000 mAh g⁻¹ for 100 cycles at 50 mA g⁻¹ and can bear a current density of 3000 mA g⁻¹ for 400 cycles without obvious capacity fading.

2. Experimental section

2.1. Synthesis of POMOFs/RGO nanocomposites and other control samples

Synthesis of POMOFs/RGO: The POMOFs/RGO nanocomposites were synthesized using PMO₁₀V₂ (Average zeta potential is -24.3 mV), Cu(OAc)₂·H₂O, H₃BTC, GO and L-ascorbic acid by a facile one-pot method (OAc=acetate) based on our previous work [31]. GO loadings are chosen as 4, 8, 12 wt%, according to the total mass of the precursors, referring as PMG-1, PMG-2, PMG-3 respectively. Firstly, PMO₁₀V₂ (0.22g, 0.092 mmol) and L-ascorbic acid (0.017g, 0.1 mmol) were mixed in distilled water (15 mL), the solution colour changed from orange to dark blue and were stirred for 10 min to form homogenous solution (solution A). Then GO (0.0764g, take 12 wt% for example) and Cu(OAc)₂·H₂O (0.2g, 1 mmol) were added to solution A under stirring for 20 min (solution B). The pH of the solution B was adjusted to 3.5 by 1 M HCl. At last, H₃BTC (0.14g, 0.67 mmol) dissolved in alcohol (10 mL) was added dropwise into the above solution with continuous stirring and the solution was refluxed for 12 h. A deep green precipitate appeared eventually. Then, the precipitate was washed through centrifugation with the mixture of distilled water and alcohol (v: v = 1:1) for 6 times until the centrifugal mother liquid is clear in order to remove the remaining reactants, such as RGO, L-ascorbic acid, H₃BTC and PMO₁₀V₂ and so on. At last POMOFs/RGO

composite was obtained after drying at 60 °C for 24 h. GO sheets were transformed to RGO nanosheets because of the reduction of L-ascorbic acid and PMO₁₀V₂ which was confirmed by the Raman spectrum (Fig. S1). For comparison, NENU-5/RGO (12 wt%) was synthesized through the same method except that H₃PMO₁₂O₄₀·nH₂O (0.17g, 0.092 mmol) was used to replace H₅[PMO₁₀V₂O₄₀]·nH₂O.

Synthesis of HKUST-1: 1.8 mM of cupric nitrate trihydrate was heated with 1.0 mM of H₃BTC in 12 mL of 50: 50H₂O: alcohol at 110 °C for 12 h in a Teflon 23-mL Parr pressure vessel. The precipitate was collected by centrifugation and washed through centrifugation with alcohol and distilled water. After drying at 60 °C for 24 h, the nanocrystalline material was obtained.

Synthesis of HKUST-1/RGO (12 wt%): Cu(OAc)₂·H₂O (0.2g, 1 mmol), 0.046g GO and L-ascorbic acid (0.017g, 0.1 mmol) was heated with H₃BTC (0.14g, 0.67 mmol) in 20 mL of 50: 50H₂O: alcohol at 110 °C for 12 h in a Teflon 23-mL Parr pressure vessel. The precipitate was collected by centrifugation and washed through centrifugation with alcohol and distilled water. After drying at 60 °C for 24 h, the nanocrystalline material was obtained.

Synthesis of PMO₁₀V₂/RGO (12 wt%): H₅[PMO₁₀V₂O₄₀]·nH₂O (0.22g, 0.092 mmol) and GO (0.03g) were dissolved in distilled water (20 mL) at 180 °C for 12 h in a 50 mL Teflon-lined stainless steel autoclave. The precipitate was collected by centrifugation and washed through centrifugation with alcohol and distilled water. After drying at 60 °C for 24 h, black PMO₁₀V₂/GO nanohybrids are obtained.

Synthesis of NENU-9: Cu(OAc)₂·H₂O (0.2g, 1 mmol) and H₅[PMO₁₀V₂O₄₀]·nH₂O (0.22g, 0.092 mmol) in distilled water (10 mL) were stirred for 20 min (solution A). The pH of the solution A was adjusted to 3.5 by 1 M HCl. H₃BTC (0.14g, 0.67 mmol) was dissolved in alcohol (10 mL), and this solution was added dropwise to solution A with continuous stirring at room temperature. A green precipitate appeared immediately. The precipitate was collected by centrifugation and washed through centrifugation with alcohol and distilled water. After drying at 60 °C for 24 h, the nanocrystalline material was obtained.

2.2. Material characterization

Zeta potential measurements were carried out with a Zetasizer nano 3600 instrument. Powder X-Ray diffraction (PXRD) patterns were recorded on a D/max 2500 VL/PC diffractometer (Japan) equipped with graphite mono-chromatized Cu K α radiation (λ =1.54060 Å). Corresponding work voltage and current is 40 kV and 100 mA, respectively. Transmission electron microscopy (TEM) and high-resolution TEM (HRTEM) images were carried out on JEOL-2100F apparatus at an accelerating voltage of 200 kV. Morphology analysis was conducted on a scanning electron microscope (SEM, JSM-7600F) at an acceleration voltage of 10 kV. Elemental mapping was performed with JSM-5160LV-Vantage typed energy spectrometer. X-ray photoelectron spectroscopy (XPS) was collected on scanning X-ray microprobe (PHI 5000 Versa, ULAC-PHI, Inc.) using Al K α radiation and the C1s peak at 284.8 eV as internal standard. Nitrogen adsorption-desorption isotherms were measured at 77 K on a Quantachrome Instruments Autosorb AS-6B.

2.3. Electrochemical characterization

The crystal water of all the as prepared powders was removed before used as the electrodes. The working electrodes were prepared by mixing 70 wt% active material, 20 wt% acetylene black (Super-P), and 10 wt% polyvinylidene fluoride (PVDF) in N-methyl-2-pyrrolidinone. After coating the above slurries on Cu foils, the electrodes were dried at 90 °C in vacuum for 6 h to remove the solvent before pressing. Then the electrodes were cut into disks (14 mm in diameter) and dried at 90 °C for 24 h in vacuum. The coin cells were laboratory-assembled by a CR 2032 press in an argon-filled glovebox where the moisture and oxygen

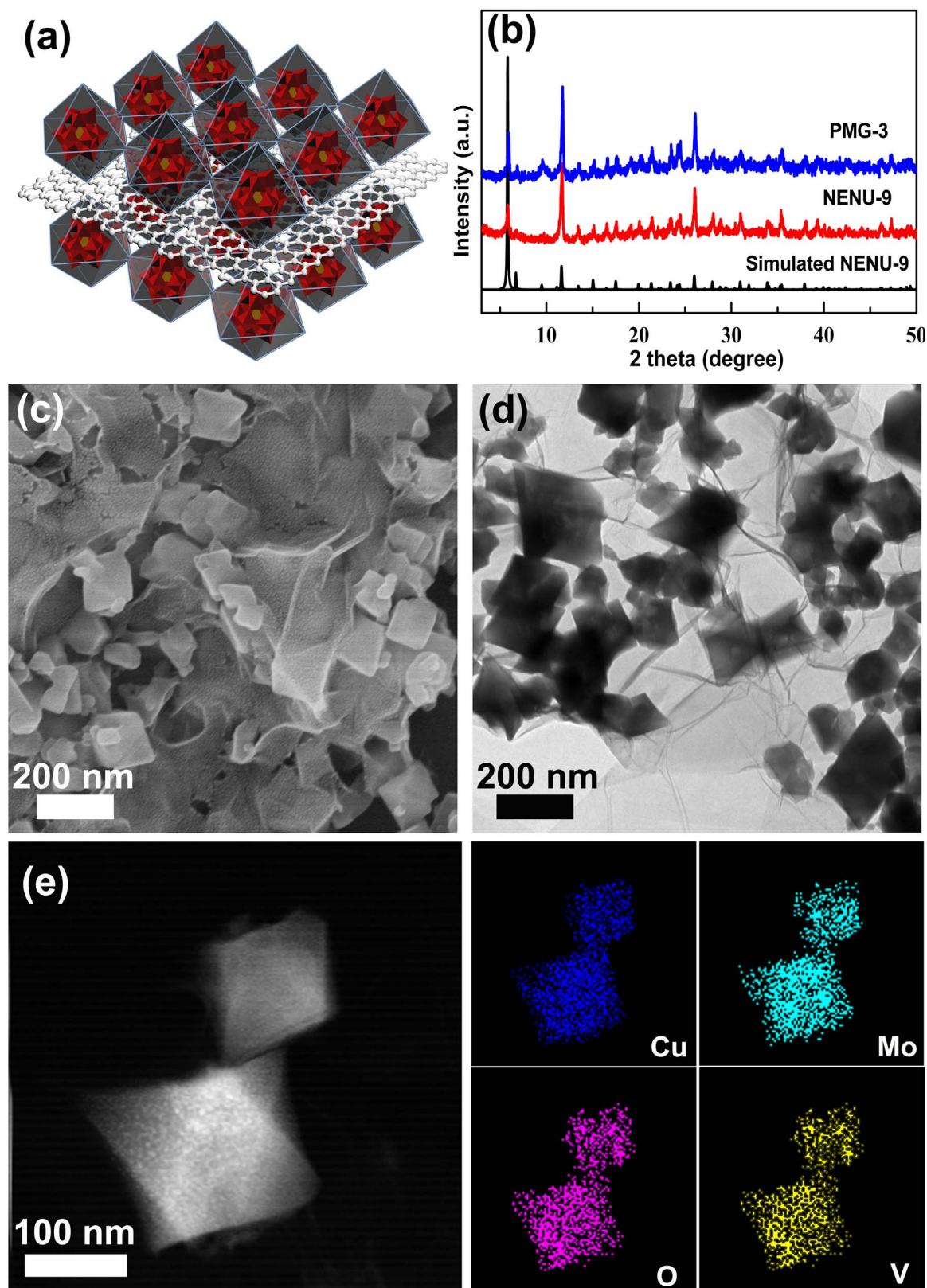


Fig. 1. (a) Schematic diagram of PMG nanocomposites. (b) PXRD patterns of as-prepared NENU-9 and PMG-3. (c) SEM image of PMG-3. (d) TEM image of PMG-3. (e) Corresponding EDX elemental mapping of Cu, Mo, O and V.

concentrations were strictly limited to below 1 ppm. A lithium foil was used as the counter electrode, and a Celgard 2400 membrane was used as the separator. The electrolyte was composed of 1 M LiPF_6 in a mixture of ethylene carbonate (EC) and dimethyl carbonate (DMC) (v :

$v = 1:1$). The galvanostatic charge/discharge tests were carried out on a Land Battery Measurement System (Land, CT2001A, China) at various current densities of 50–3000 mA g^{-1} with a cut off voltage of 3–0.01 V vs Li^+/Li at room temperature. The specific capacity was calculated

based on the mass of active material.

Electrochemical impedance spectroscopy (EIS) measurements and Cyclic voltammetry (CV) were conducted on CHI 660D (Shanghai, China) electrochemical workstation at room temperature. EIS measurements were carried out in the frequency range from 100 kHz to 0.01 Hz with an amplitude of 5 mV at various voltage. CV curves were obtained at a scan rate of 0.02–10 mV s⁻¹ in the range from 3 to 0.01 V.

3. Results and discussion

The schematic diagram of PMG nanocomposites is shown in Fig. 1a. For PMG nanocomposites, the structure of POMOF is same to NENU-9 ([Cu₂(BTC)_{4/3}]₆[H₅PMo₁₀V₂O₄₀]) [32]. Crystallographic studies revealed that each paddle-wheel unit Cu₂-cluster is bridged four BTC ligands (Fig. S2a) to generate a 3D network (Fig. S2b). Meanwhile, the keggin-type POMs (PMo₁₀V₂) are introduced into the pores of the 3D framework (Fig. S2c), which is isostructural to previously reported NENU-*n* (*n*=1–6) which immobilized different POMs [33].

The powder X-ray diffraction (PXRD) was used to characterize the structures of PMG-3, NENU-9 (Fig. 1b), HKUST-1 and HKUST-1/RGO (Fig. S3), all of these as-prepared samples are in good agreement with the corresponding simulated patterns, confirming the phase purity and good crystallinity. As shown in Fig. 1c and d, scanning electron microscopy (SEM) and transmission electron microscopy (TEM) images of PMG-3 reveal the unique structures that the octahedral POMOFs nanoparticles with ~200 nm in size are uniformly loaded on RGO nanosheets. NENU-9 particles without RGO loadings also show similar octahedral morphology and nano- sizes (Fig. S4). In addition, elemental mapping has been conducted to obtain the elemental distribution of Cu, Mo, O, and V of PMG-3 (Fig. 1e), which are in accord with the structure of POMOFs.

Nitrogen (N₂) adsorption-desorption isotherms are also used to evaluate the porous structures of HKUST-1, NENU-9 and PMG-3, respectively (Fig. S5). The PMG-3 has the type IV isotherm with the hysteresis loops at the relatively high pressure range, which indicating the mesoporous structures resulting from the stacking of POMOFs and RGO films. In addition, the contributions of micropores of PMG-3 can be observed at relatively low pressures, which originate from pores of POMOFs. In contrast, the type I isotherms for HKUST-1 and NENU-9 both demonstrate their microporous structures. It is worth mentioning that the adsorption volume of NENU-9 is lower than HKUST-1, indicating the successful encapsulation of POMs into the pores of MOFs. Furthermore, the decreases of the adsorption volume for PMG-3 suggest the combination of RGO films and POMOFs when comparing with NENU-9. The specific surface area or HKUST-1, NENU-9 and PMG-3 are 1417.8, 770.4 and 286.9 m² g⁻¹, respectively.

The compositions and element valences of PMG-3 before and after discharged at 0.01 V were investigated by the X-ray photoelectron spectroscopy (XPS). The survey spectrums of both samples demonstrate the existence of C, Cu, Mo, P, V and O elements (Fig. 2a and e). The high-resolution C1s spectrum of both samples could be deconvoluted into three Gaussian peaks associated with C–C, C–O, and C⁺O, respectively (Fig. 2b and f) [34,35]. Before test, the Mo3d spectrum of PMG-3 in Fig. 2c has the two main peaks at 232.3 eV and 235.5 eV, which could be assigned to Mo⁶⁺3d_{5/2} and Mo⁶⁺3d_{3/2} of MoO₃, respectively [34]. After discharged to 0.01 V, parts of Mo⁶⁺ are reduced to Mo⁴⁺ because of the appearance of Mo⁴⁺ peaks at the binding energy of 231.9 eV (Fig. 2g) [36]. In addition, as can be seen in Fig. 2d, Cu2p spectra has the two main peaks of Cu2p_{3/2} (932.6 eV) and Cu2p_{1/2} (952.6 eV) with strong shake-up satellite peaks at about 941.0 eV, demonstrate the existence of Cu²⁺ [37]. After discharged to 0.01 V, the peaks of Cu2p_{3/2} and Cu2p_{1/2} located at 932.5 and 952.7 eV also corresponding to Cu²⁺ state (Fig. 2h) [38].

The electrochemical performances of the synthesized composites were evaluated by assembling them into coin cells with lithium as

counter electrode and cycled between 3.0 and 0.01 V vs Li⁺/Li. Fig. 3a shows the comparative cycling performances of the PMG-1 to PMG-3 at a current density of 50 mA g⁻¹. PMG-3 shows the highest capacity over all the tested cycles. The first discharge and charge capacities of PMG-3 are 2367.8 and 1519.8 mAh g⁻¹, acquiring an initial Coulombic efficiency (CE) of 64.1%, which is better than PMG-1 (56.2%) and PMG-2 (57.2%). The initial irreversible capacity loss is mainly due to the decomposition of the electrolyte and subsequent formation of the solid electrolyte interphase (SEI) film, and the reaction of remaining oxygen-containing functional groups on RGO with lithium ions [4]. Such initial irreversible loss of lithium has been a common phenomenon in LIBs [4,7,9]. After the first few cycles, the CE of PMG-3 quickly improves to above 99%. After 100 cycles, the reversible capacities of PMG-1, PMG-2 and PMG-3 are stabilized at 605, 802 and 1075 mAh g⁻¹ respectively, all the PMG nanocomposites demonstrate excellent cycling stability. The capacity of PMG-3 is also among the best compared to other pristine (not used as a template, such as carbonation) POMs or MOFs based anodes that have been reported so far (Table S1). Electrochemical impedance spectra (EIS) of the PMG electrodes and NENU-9 were also conducted (Fig. S6). The conductivities of the PMG electrodes are 4 orders of magnitude higher than that of NENU-9 electrode without RGO. And also the PMG-3 shows the smallest resistance and the resistances of the PMG-1 to PMG-3 decrease with increasing RGO loadings, which indicating an enhanced conductivity to the PMG nanocomposites by RGO. During our research, we also tried to synthesis the nanocomposite with higher GO content (14%), however, its cycling performance is poorer than PMG-3 (Fig. S7). This is because higher GO content may lead to the inhomogeneous nanocomposites, thus 12% was chosen as the highest GO content in this study.

For comparison, the cycling performances of HKUST-1, PMo₁₀V₂, NENU-9 (PMo₁₀V₂@HKUST-1), HKUST-1/RGO and PMo₁₀V₂/RGO were also tested (Fig. S8), the GO loadings of HKUST-1/RGO and PMo₁₀V₂/RGO are all 12 wt%, same to PMG-3. There is an increasing trend at the first few cycles for most of the samples, this may be attributed to the activation of the electrodes and improvement in Li⁺ insertion-deinsertion processes with repeated cycling. After 100 cycles, the reversible capacities of all the samples are listed in Table S2. Compared Fig. 3a with Fig. S8, PMG-3 also shows the highest reversible capacity and the best cycling stabilities, indicating that POMOFs/RGO nanostructures are superior to not only any single component but also two of the HKUST-1, PMo₁₀V₂ and RGO (PMo₁₀V₂@HKUST-1, PMo₁₀V₂/RGO and HKUST-1/RGO). It can be concluded that the POMOFs/RGO nanostructures can combine the advantages of POMs, MOFs and RGO by the synergistic effects of the three.

We also tried to explore electrodes based on POMOFs/RGO with different keggin-type POMs for LIBs. NENU-5/RGO was synthesized for its structure (Fig. S9a) and compositions are similar to that of PMG-3 except for PMo₁₀V₂ was replaced by PMo₁₂. NENU-5/RGO also shows acceptable cycling performance and reversible capacity (about 860 mAh g⁻¹) after 100 cycles (Fig. S9b), which is superior than most of other POMs or MOFs-based electrodes. However, this performance is poorer than PMG-3, maybe for the reason that the oxidizing ability (V⁵⁺ > Mo⁶⁺) [30,39,40]. Whatever, the conclusion can be drawn that POMOFs/RGO nanostructures might open up the possibilities for designing advanced electrode materials based on different POMOFs.

Considering PMG-3 shows the best performances, PMG-3 was used for further studies in the following works. The charge/discharge profiles of the PMG-3 anode for cycle number of 1, 2, 10, 20 and 50 are shown in Fig. 3b, due to the formation of the SEI film, the 1st discharge process is different from the others. After that, the curves almost overlapped which indicates the formation of a stable SEI film and a good electrochemical reversibility of the electrode. Cyclic voltammetry (CV) of PMG-3 in the range of 0.01 – 3.0 V at a scan rate of 0.2 mV s⁻¹ for different cycles are shown in Fig. 3c. In the first

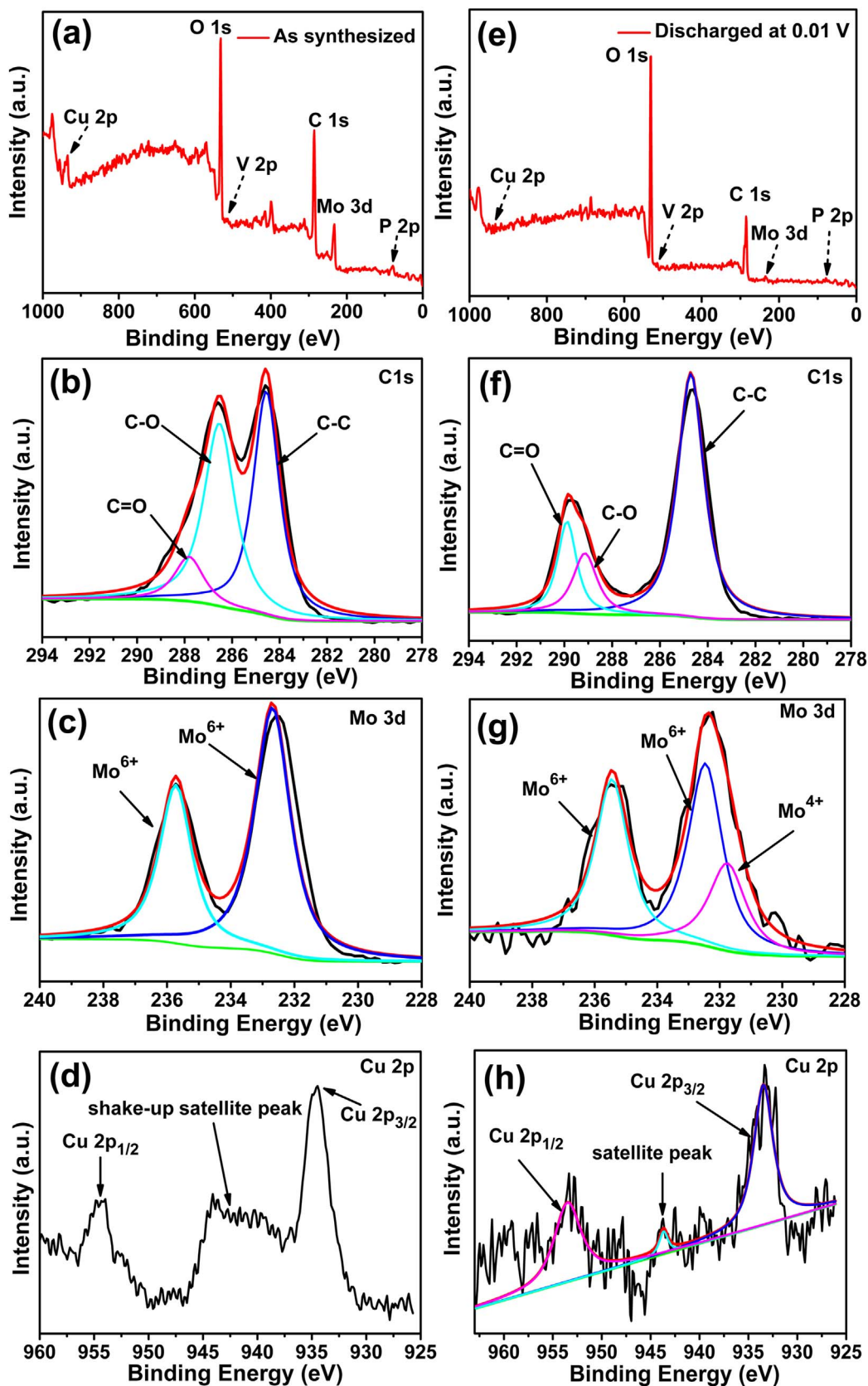


Fig. 2. XPS spectra of PMG-3 before and after discharged at 0.01 V. (a) - (d): As synthesized powders, (a) survey scan. (b) C 1 s (c) Mo 3d. (d) Cu 2p; (e) - (f): Discharged at 0.01 V, (e) survey scan. (f) C 1 s (g) Mo 3d. (h) Cu 2p.

discharge, i.e., the process of inserting Li^+ into the PMG-3 structure, an irreversible cathodic peak at around 0.62 V is also attributed to the SEI formation. In the subsequent cycles, two indistinct peaks become

visible at the potential of 1.25 V for the reduction and 1.50 V for the oxidation, indicating a defined electrochemical process, which may be ascribe to the reduction and oxidation of the Mo (XPS results in

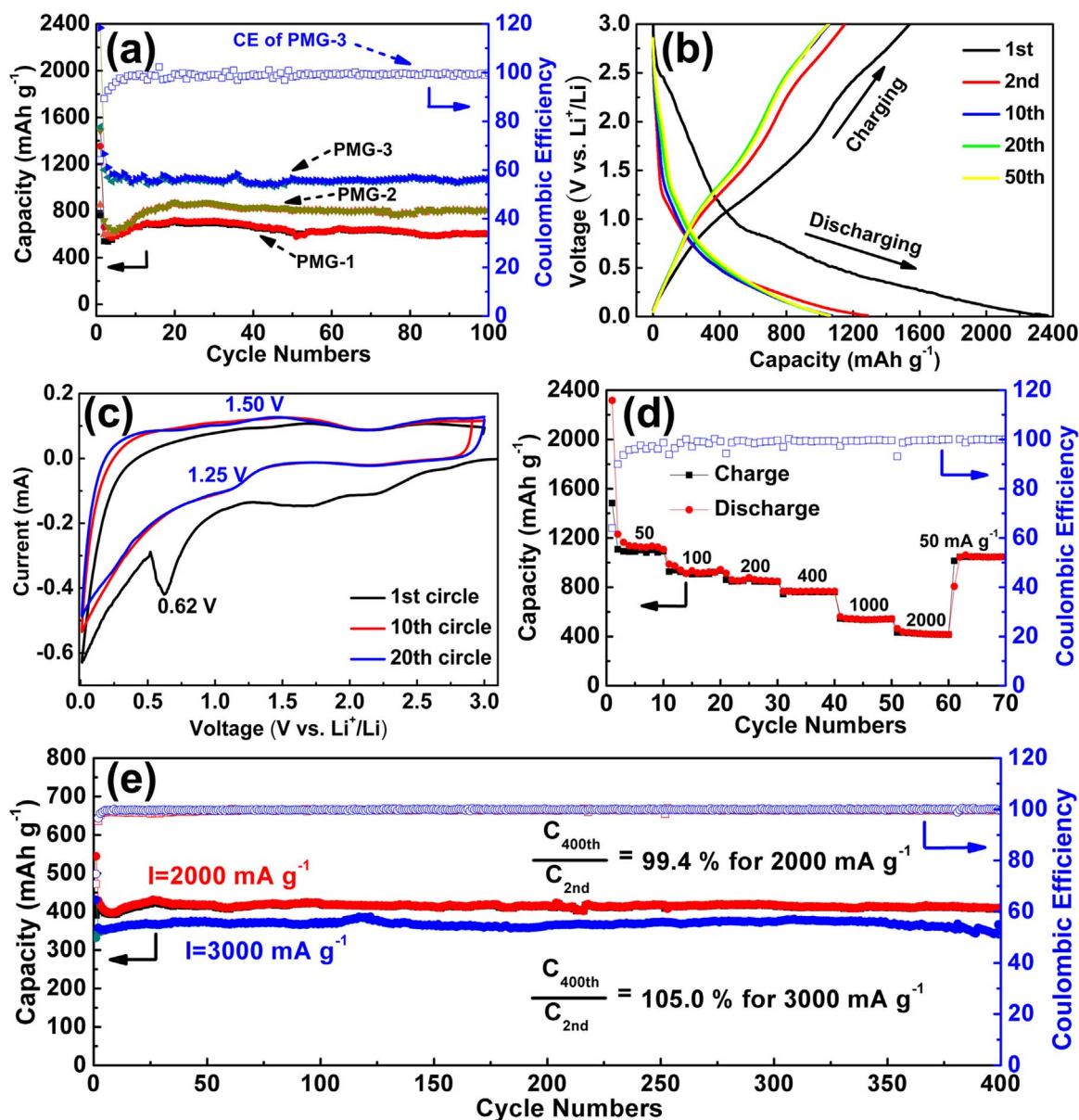


Fig. 3. Electrochemical performances of PMG anodes. The specific capacity was calculated based on the mass of active material. (a) Cycling performance of PMG-1 to PMG-3 at a current density of 50 mA g⁻¹. (b) Charge/discharge profiles of PMG-3 for different cycles constantly at 50 mA g⁻¹. (c) CV profiles of PMG-3 at a scan rate of 0.2 mV s⁻¹. (d) PMG-3 cycled at various current densities. (e) Stability test of PMG-3 for 400 cycles at 2000 mA g⁻¹ and 3000 mA g⁻¹, respectively.

Fig. 2g). The indistinct peaks here in the CV profiles, are similar to the pseudocapacitive materials [4,7,9,41].

The PMG-3 electrode can be also reversibly cycled at various current densities (Fig. 3d), the average specific capacities are approximately 1088, 906, 846, 761, 538 and 428 mAh g⁻¹ at the current densities of 50, 100, 200, 400, 1000 and 2000 mA g⁻¹, respectively. When the current density is reduced back to 50 mA g⁻¹, a high capacity of 1046 mAh g⁻¹ is immediately resumed, suggesting the good reversibility of the PMG-3 electrode. Further, at higher current densities of 2000 and 3000 mA g⁻¹ (Fig. 3e), the PMG-3 electrodes can also deliver capacities of 409 and 365 mAh g⁻¹ respectively, for over 400 cycles without obvious capacity fading. More specifically, by comparing the capacity of 400th cycle with the 2nd cycle, the capacity retentions at 2000 and 3000 mA g⁻¹ are 99.4% and 105.0% respectively, demonstrating superior cycling and rate performances. This cycling stability is also the best of the pristine MOFs and POMs based electrodes that ever reported (Table S1) and even comparable with some excellent MOF-derived electrodes, such as ZnO@ZnO quantum

dots/C [42] and CoS_x/RGO [43]. This ultra-stability may benefit from the open framework of MOFs which could mechanically buffer the volume change of the POMs and prevent the POMs particles detaching from the electrode, thus eventually stabilizing the PMG structure. What's more, XRD results show that the original structure of PMG-3 is still retained after 100 cycles (Fig. 4), indicating that the PMG nanostructures are stable up to a certain concentration of Li⁺. This result may also contribute to the ultra-stability of the PMG-3 electrode.

It is extremely “surprising” to achieve such unprecedentedly performances for pristine POMs/RGO nanocomposites in terms of high reversible capacity, excellent cycling stability, and good rate capability. The large reversible capacity (1075 mAh g⁻¹ at 50 mA g⁻¹) of PMG-3 is nearly three times of the theoretical capacity of graphite (≈372 mAh g⁻¹) and is also much higher than the theoretical capacity of graphene (≈744 mAh g⁻¹). We calculated the theoretical capacity of NENU-9 (≈449 mAh g⁻¹) based on: (1) Redox reactions of metal ions in PMo₁₀V₂ (Mo⁶⁺ to Mo⁴⁺, V⁵⁺ to V⁴⁺) which are due to the

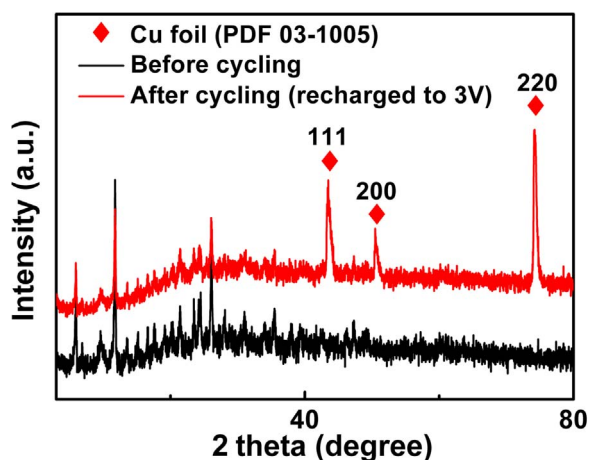


Fig. 4. XRD patterns of PMG-3 before and after cycling. XRD samples of the electrodes after cycling were disassembled in the glove box. Then the working electrode was taken out of the cell and rinsed several times with DMC before being vacuum-dried for 12 h at room temperature. At last the working electrodes were directly tested on the Cu foil.

intercalation mechanism for Li storage. (2) Possible lithiation/delithiation sites for coordination with Li in the organic moiety of the HKUST-1 [44]. Mo^{6+} to Mo^{4+} is based on the XPS results and studies [25,26], V^{5+} to V^{4+} according to studies [40,45] (Calculations can be seen in the Supporting information). Obviously, this value highly exceeds the theoretical value, similar results were also discovered in $\text{TBA}_3[\text{PMo}_{12}\text{O}_{40}]/\text{RGO}$ electrodes by Awaga et al. [46] Dunn et al. pointed out that the access capacity in LIBs is caused by an interfacial Li storage mechanism that is, capacitive behavior, which includes both the non-Faradaic electrical double layer capacitance (EDLC) and the pseudocapacitance [5,6,47,48], most studies agrees with their theory in

recent years [4–7,47,48], we also try to explain the extra capacity here by using Dunn's methods.

To confirm whether the capacity contributed by the capacitive behavior or not, CV profiles of PMG-3 at different scan rates ($0.2\text{--}10\text{ mV s}^{-1}$) were recorded between $0.01\text{--}3.0\text{ V}$ (Fig. 5a). It can be explained using the power law $i = a\nu^b$, where ν is the scan rate, and both a and b are adjustable parameters [4–7,47,48]. In general, when $b = 0.5$, it means that the electrode reaction is diffusion-controlled and satisfies Cottrell's equation: $i = a\nu^{0.5}$. While for the reaction which is limited by surface process, $b = 1$. The parameter b can be determined from the slope of the linear plot of $\log i$ versus $\log \nu$ (Fig. 5b). It is noteworthy that when the scan rate was increased from 0.2 to 10 mV s^{-1} , the b value at 1.2 V was determined to be 0.66 , indicating the dominance of the diffusion-controlled lithium storage process, whereas the b value was 0.94 at 0.1 V , revealing a surface-controlled charge storage behavior.

With this in view, it is important to distinguish quantitatively the capacitive contribution. We can write the equations like below (equation 1 or 2), i.e., the current response “ i ” at a given potential “ V ” is the sum of two contributions arising from the capacitance and intercalation capacity [4–7,47,48].

$$i(V) = k_1\nu + k_2\nu^{0.5} \quad (1)$$

or

$$i(V)/\nu^{0.5} = k_1\nu^{0.5} + k_2 \quad (2)$$

where $k_1\nu$ and $k_2\nu^{0.5}$ correspond to the current contributions from the capacitive (EDLC and pseudocapacitance) and diffusion processes (intercalation), respectively. Thus, it is possible to determine the current response due to capacitive and diffusion processes at a given potential by determining k_1 and k_2 . In Fig. 5c, the voltage profile for the capacitive current response is shown as a shaded area in comparison

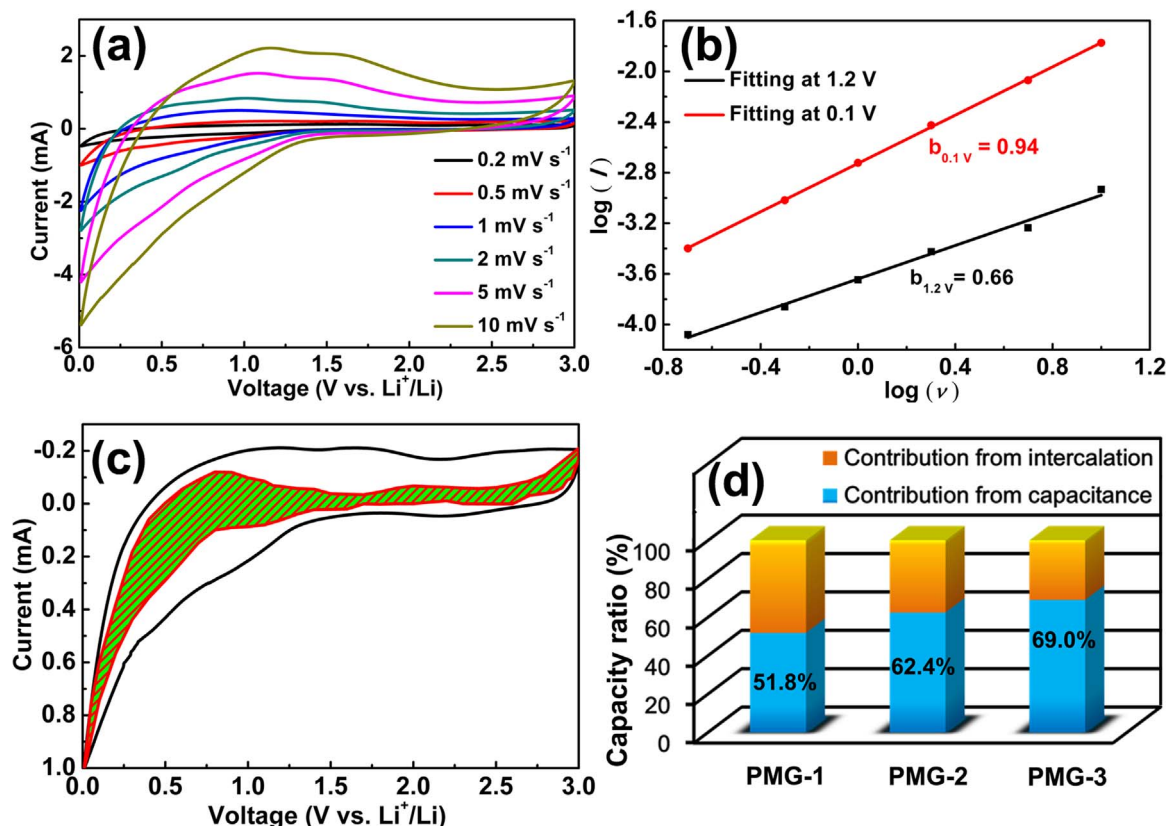


Fig. 5. Evaluation the capacity contributed by the capacitive behavior. (a) CV curves of PMG-3 at various scan rates, from 0.2 to 10 mV s^{-1} . (b) b -value determination of 1.2 V and 0.1 V cathodic current. (c) Capacitive-controlled charge storage contributions separated with cyclic voltammogram at 0.5 mV s^{-1} scan. (d) Comparison of capacity ratio for PMG nanocomposites (0.5 mV s^{-1} sweep rate). The total capacity is separated into lithium intercalation and capacitive contributions.

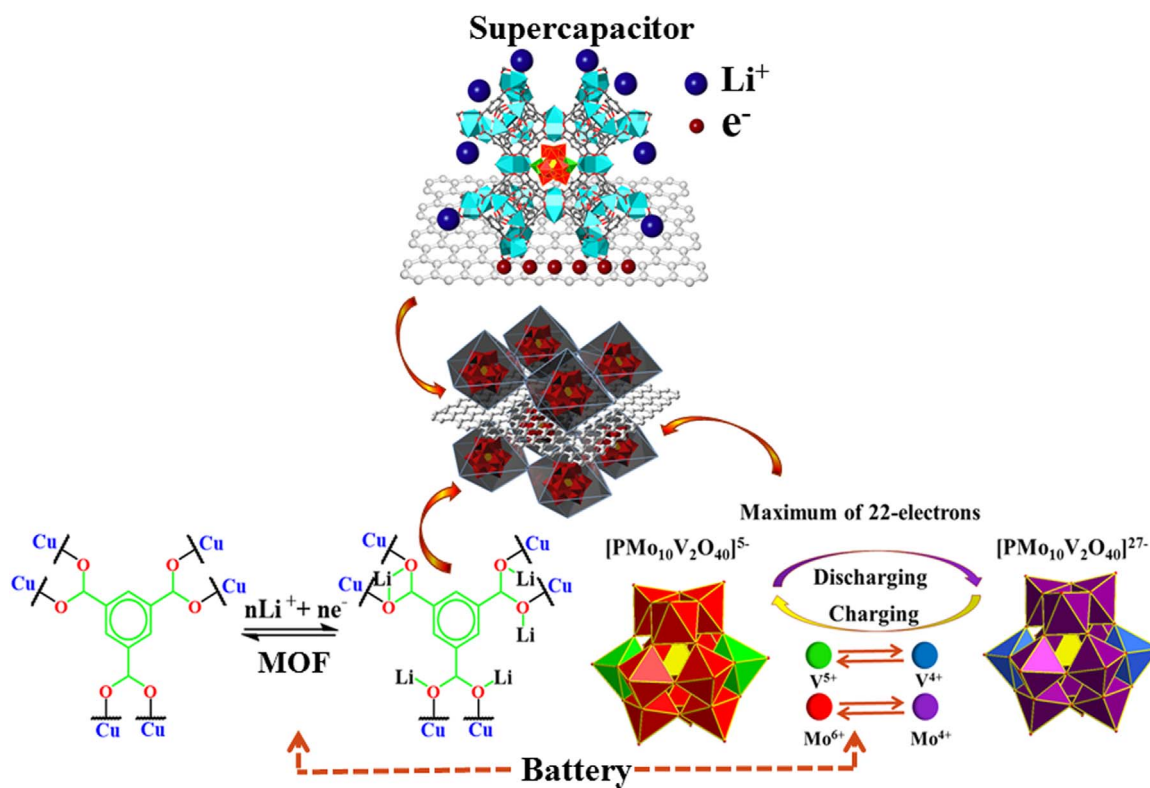


Fig. 6. The schematic diagram of the possible mechanism for the cooperative capacity of battery-supercapacitor for the PMG nanocomposites.

with the total measured current on a typical CV for PMG-3 at the scan rate of 0.5 mV s^{-1} (PMG-1 and PMG-2 are seen in Fig. S10). The results show that the capacitive-controlled capacity makes up about 69.0% of the total capacity for PMG-3, whereas this value decreases to about 62.4% and 51.8% for PMG-2 and PMG-1, respectively (Fig. 5d), which indicates the significant role of the capacitive contribution in the total capacity, especially at higher RGO loadings. Thus, a kind of high-capacity and high-rate LIBs with these novel PMG nanocomposites, in which surface and diffusion-controlled lithium storage are achieved.

Based on the discussion above, a possible mechanism for the cooperative capacity of battery-supercapacitor behavior was proposed below (Fig. 6). The battery behaviors of HKUST-1 and $\text{PMo}_{10}\text{V}_2$ are achieved by coordination with Li^+ in the organic moiety of MOFs and redox of metal ions (Mo and V) of the POMs, respectively. At the same time, capacitive behaviors may be realized like this: in addition to the Li^+ which are inserted into the lattice of POMOFs (pseudocapacitance), there are additional Li^+ stored in the accessible interstitial sites on the interface or pores of POMOFs, charge compensated by additional electrons on the RGO surface. Thus, the PMG nanocomposites may provide a new and efficient platform for developing electrode materials of LIBs with hybrid behavior of battery and supercapacitor.

4. Conclusions

In summary, this study demonstrates the utilization of PMG nanocomposites as anode materials for rechargeable LIBs for the first time. It shows the cooperative capacity of battery-supercapacitor behavior for superior lithium storage by combine the advantages of the POMs, MOFs and RGO together, such as multi-electron redox properties of POMs, high electronic conductivity of RGO and open frameworks of MOFs which can buffer the volume expansion and ensure good cycling stabilities. Compared to the pristine MOFs and POMs based electrodes reported yet, this nanocomposites show the largest reversible capacity of 1075 mAh g^{-1} and the capacity retentions are nearly 100% both at 2000 and 3000 mA g^{-1} for over 400 cycles.

What's more, XRD results show that the original structure of PMG-3 is still retained after 100 cycles. The significant improvement of performances might guide the design of advanced electrode materials based on different POMOFs nanocomposites for Li- and Na-storage, even for supercapacitors.

Acknowledgements

This work was financially supported by the National Natural Science Foundation of China (No. 21622104, 21371099 and 21471080), the NSF of Jiangsu Province of China (No. BK20141445), the Priority Academic Program Development of Jiangsu Higher Education Institutions, the Foundation of Jiangsu Collaborative Innovation Center of Biomedical Functional Materials and Jiangsu Planned Projects for Postdoctoral Research Funds (1601087 C).

Appendix A. Supplementary material

Supplementary data associated with this article can be found in the online version at doi:10.1016/j.nanoen.2017.02.028.

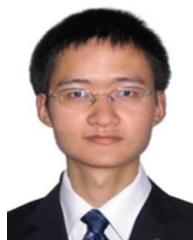
References

- [1] M. Armand, J.M. Tarascon, *Nature* 451 (2008) 652–657.
- [2] N. Armaroli, V. Balzani, *Energy Environ. Sci.* 4 (2011) 3193–3222.
- [3] B. Dunn, H. Kamath, J.M. Tarascon, *Science* 334 (2011) 928–935.
- [4] T.Z. Yuan, Y.Z. Jiang, W.P. Sun, B. Xiang, Y. Li, M. Yan, B. Xu, S.X. Dou, *Adv. Funct. Mater.* 26 (2016) 2198–2206.
- [5] P. Simon, Y. Gogotsi, B. Dunn, *Science* 343 (2014) 1210–1211.
- [6] V. Augustyn, P. Simon, B. Dunn, *Energy Environ. Sci.* 7 (2014) 1597–1614.
- [7] J.Y. Wang, H.J. Tang, L.J. Zhang, H. Ren, R.B. Yu, Q. Jin, J. Qi, D. Mao, M. Yang, Y. Wang, P. Liu, Y. Zhang, Y.R. Wen, L. Gu, G.H. Ma, Z.G. Su, Z.Y. Tang, H.J. Zhao, D. Wang, *Nat. Energy* 1 (2016) 16050–16057.
- [8] M. Sathya, A.S. Prakash, K. Ramesha, J.M. Tarascon, A.K. Shukla, *J. Am. Chem. Soc.* 133 (2011) 16291–16299.
- [9] L.L. Tian, M.J. Zhang, C. Wu, Y. Wei, J.X. Zheng, L.P. Lin, J. Lu, K. Amine, Q.C. Zhuang, F. Pan, *ACS Appl. Mater. Interfaces* 7 (2015) 26284–26290.
- [10] D.W. Su, K. Kretschmer, G.X. Wang, *Adv. Energy Mater.* 6 (2016) 1501785.

- [11] G. Zhou, F. Li, H.M. Cheng, *Energy Environ. Sci.* 7 (2014) 1307–1338.
 [12] L. Croguennec, M.R. Palacin, *J. Am. Chem. Soc.* 137 (2015) 3140–3156.
 [13] O.M. Yaghi, G. Li, H. Li, *Nature* 378 (1995) 703–706.
 [14] S.L. Li, Q. Xu, *Energy Environ. Sci.* 6 (2013) 1656–1683.
 [15] F.S. Ke, Y.S. Wu, H. Deng, *J. Solid State Chem.* 223 (2015) 109–121.
 [16] L. Wang, Y.Z. Han, X. Feng, J.W. Zhou, P.F. Qi, B. Wang, *Coord. Chem. Rev.* 307 (Part 2) (2016) 361–381.
 [17] F. Xu, Z.W. Tang, S.Q. Huang, L.Y. Chen, Y.R. Liang, W.C. Mai, H. Zhong, R.W. Fu, D.C. Wu, *Nat. Commun.* 6 (2015) 7221.
 [18] C.D. Wessells, R.A. Huggins, Y. Cui, *Nat. Commun.* 2 (2011) 550.
 [19] W. Li, J. Liu, D. Zhao, *Nat. Rev. Mater.* 1 (2016) 16023.
 [20] F. Zheng, Y. Yang, Q. Chen, *Nat. Commun.* 5 (2014) 6261.
 [21] Y.F. Yue, B.K. Guo, Z.A. Qiao, P.F. Fulvio, J.H. Chen, A.J. Binder, C.C. Tian, S. Dai, *Micro Meso. Mater.* 198 (2014) 139–143.
 [22] G. Ferey, F. Millange, M. Morcrette, C. Serre, M.L. Doublet, J.M. Greneche, J.M. Tarascon, *Angew. Chem. Int. Ed.* 46 (2007) 3259–3263.
 [23] K.M. Choi, H.M. Jeong, J.H. Park, Y.B. Zhang, J.K. Kang, O.M. Yaghi, *Acs Nano* 8 (2014) 7451–7457.
 [24] J.J. Chen, M.D. Szymes, S.C. Fan, M.S. Zheng, H.N. Miras, Q.F. Dong, L. Cronin, *Adv. Mater.* 27 (2015) 4649–4654.
 [25] H. Wang, S. Hamanaka, Y. Nishimoto, S. Irle, T. Yokoyama, H. Yoshikawa, K. Awaga, *J. Am. Chem. Soc.* 134 (2012) 4918–4924.
 [26] Y. Nishimoto, D. Yokogawa, H. Yoshikawa, K. Awaga, S. Irle, *J. Am. Chem. Soc.* 136 (2014) 9042–9052.
 [27] Y.Y. Chen, M. Han, Y.J. Tang, J.C. Bao, S.L. Li, Y.Q. Lan, Z.H. Dai, *Chem. Commun.* 51 (2015) 12377–12380.
 [28] G.J. Suarez, V. Ruiz, R.P. Gomez, *Phys. Chem. Chem. Phys.* 16 (2014) 20411–20414.
 [29] Y.F. Yue, Y.C. Li, Z.H. Bi, G.M. Veith, C.A. Bridges, B.K. Guo, J. Chen, D.R. Mullins, S.P. Surwade, S.M. Mahurin, H.J. Liu, M.P. Paranthaman, S. Dai, *J. Mater. Chem. A* 3 (2015) 22989–22995.
 [30] M. Sadakane, E. Steckhan, *Chem. Rev.* 98 (1998) 219–238.
 [31] Y.J. Tang, M.R. Gao, C.H. Liu, S.L. Li, H.L. Jiang, Y.Q. Lan, M. Han, S.H. Yu, *Angew. Chem. Int. Ed.* 54 (2015) 12928–12932.
 [32] Y.W. Liu, S.M. Liu, S.X. Liu, D.D. Liang, S.J. Li, Q. Tang, X.Q. Wang, J. Miao, Z. Shi, Z.P. Zheng, *Chemcatchem* 5 (2013) 3086–3091.
 [33] C.Y. Sun, S.X. Liu, D.D. Liang, K.Z. Shao, Y.H. Ren, Z.M. Su, *J. Am. Chem. Soc.* 131 (2009) 1883–1888.
 [34] J.J. Xie, Y. Zhang, Y.L. Han, C.L. Li, *Acs Nano* 10 (2016) 5304–5313.
 [35] H.L. Tai, Z. Yuan, W.J. Zheng, Z.B. Ye, C.H. Liu, X.S. Du, *Nanoscale Res. Lett.* (2016) 11.
 [36] X.F. F. ia, X.L. Hu, Y.M. Sun, W. Luo, Y.H. Huang, *Nanoscale* 4 (2012) 4707–4711.
 [37] C. Wang, J.W. Zhu, S.M. Liang, H.P. Bi, Q.F. Han, X.H. Liu, X. Wang, *J. Mater. Chem. A* 2 (2014) 18635–18643.
 [38] M. Yin, C.K. Wu, Y.B. Lou, C. Burda, J.T. Koberstein, Y.M. Zhu, S. O'Brien, *J. Am. Chem. Soc.* 127 (2005) 9506–9511.
 [39] D.M. Fernandes, A.S. Barbosa, J. Pires, S.S. Balula, L. Cunha-Silva, C. Freire, *ACS Appl. Mater. Interfaces* 5 (2013) 13382–13390.
 [40] D.M. Fernandes, C. Freire, *ChemElectroChem* 2 (2015) 269–279.
 [41] S. Hartung, N. Bucher, H.Y. Chen, R. Al-Oweini, S. Sreejith, P. Borah, Y.L. Zhao, U. Kortz, U. Stimming, H.E. Hoster, M. Srinivasan, *J. Power Sources* 288 (2015) 270–277.
 [42] G.H. Zhang, S.C. Hou, H. Zhang, W. Zeng, F.L. Yan, C.C. Li, H.G. Duan, *Adv. Mater.* 27 (2015) 2400–2405.
 [43] D.M. Yin, G. Huang, F.F. Zhang, Y.L. Qin, Z.L. Na, Y.M. Wu, L.M. Wang, *Chem. Eur. J.* 22 (2016) 1467–1474.
 [44] S. Maiti, A. Pramanik, U. Manju, S. Mahanty, *ACS Appl. Mater. Interfaces* 7 (2015) 16357–16363.
 [45] G. Bajwa, M. Genovese, K. Lian, *Ecs J. Solid State Sc.* 2 (2013) M3046–M3050.
 [46] K. Kume, N. Kawasaki, H. Wang, T. Yamada, H. Yoshikawa, K. Awaga, *J. Mater. Chem. A* 2 (2014) 3801–3807.
 [47] M.R. Lukatskaya, B. Dunn, Y. Gogotsi, *Nat. Commun.* 7 (2016) 12647.
 [48] J. Wang, J. Polleux, J. Lim, B. Dunn, *J. Phys. Chem. C.* 111 (2007) 14925–14931.



Mi Zhang received her B.S. degree from JiangXi Normal University in 2015, She is currently pursuing her M.S. degree in Nanjing Normal University. Her research interest is the preparation of polyoxometalates-based nanocomposites and its relevant applications, such as Lithium ion batteries, Sodium-ion batteries and Lithium-Sulfur batteries.



Ping Wu received his B.S. degree in 2007 and Ph. D. degree in 2012 both in Materials Science and Engineering from Zhejiang University under the supervision of Professor De-Ren Yang. He is currently an Associate Professor in School of Chemistry and Materials Science at Nanjing Normal University. His current research focuses on advanced electrode/electrocatalysis materials for energy-related applications.



Yu-Jia Tang received her undergraduate degree from Nanjing Normal University in 2013, and now she is a Ph.D. candidate in Nanjing Normal University. Her current research is mainly focused on the synthesis of polyoxometalates-based nanocomposites and their electrochemical applications, such as electrolysis of water, oxygen reduction reaction and CO₂ reduction.



Shun-Li Li was born in 1979 in Jilin, PR China. She received her B.S. (2002) in Chemistry and Ph.D. degree (2008) from Northeast Normal University under the supervision of Prof. Jian-Fang Ma. She carried out postdoctoral studies with Prof. Zhong-Min Su in Environmental Chemistry at NENU. Then she worked as a JSPS (Japan Society for the Promotion of Science) invited fellow at AIST (National Institute of Advanced Industrial Science and Technology) in 2012. She is an associate professor of Chemistry at Nanjing Normal University. Her current research interest lies in the syntheses, structures and properties of polyoxometalate-based materials.



Feng-Cui Shen received her undergraduate degree from Nanjing University of Science and Technology in 2009. Since then, she has been a teacher at Anhui Polytechnic University and now she is a Ph.D.candidate in Nanjing Tech University. Her current research is mainly focused on the synthesis of polyoxometalates-based nanocomposites for electrode material, such as lithium battery, oxygen evolution reaction and electrolysis of water.



Tao Wei received his B.S. degree in 2009 and Ph. D. degree in 2015 from China University of Mining and technology and now he is carrying out postdoctoral studies with Prof. Ya-Qian Lan in POM Chemistry at Nanjing Normal University. His current research is mainly focused on the synthesis of polyoxometalates-based MOFs and their electrochemical applications in lithium and sodium-ion batteries.



Xiao-Li Wang received her undergraduate degree from Taiyuan Normal University in 2015, and now she is a postgraduate in Nanjing Normal University. Her current research focuses on the development of polyoxometalates-based hybrid electrocatalysts for hydrogen and oxygen evolution reactions.



Ya-Qian Lan was born in 1978 in Jilin, PR China. He received his B.S. and Ph.D. degree (2009) from Faculty of Chemistry, Northeast Normal University under the supervision of Prof. Zhong-Min Su. In 2010, he worked as a JSPS postdoctoral fellow at AIST. Since the fall of 2012, he has been a Professor of Chemistry at Nanjing Normal University. His current research interests focus on the application of polyoxometalate-based composite materials in energy storage and conversion and porous metal-organic frameworks for applications in catalysis and proton conduction.



Xin-Ping Zhou is a postgraduate in China University of Mining and technology. Her current research focuses on the development of oxides based materials and interfacial electrochemistry both in lithium batteries and fuel cells.